

See discussions, stats, and author profiles for this publication at: <https://www.researchgate.net/publication/271446244>

Pt–Au–Co Alloy Electrocatalysts Demonstrate Enhanced Activity and Durability towards Oxygen Reduction Reaction

ARTICLE in ACS CATALYSIS · JANUARY 2015

Impact Factor: 9.31 · DOI: 10.1021/cs501710b

CITATIONS

2

READS

97

6 AUTHORS, INCLUDING:



Sagar Prabhudev

McMaster University

18 PUBLICATIONS 49 CITATIONS

SEE PROFILE

Pt–Au–Co Alloy Electrocatalysts Demonstrating Enhanced Activity and Durability toward the Oxygen Reduction Reaction

XueHai Tan,^{*,†} Sagar Prabhudev,[‡] Alireza Kohandehghan,[§] Dimitre Karpuzov,^{||} Gianluigi A. Botton,[‡] and David Mitlin^{*,†,§}

[†]Department of Chemical and Materials Engineering, University of Alberta, Edmonton, Alberta, Canada T6G 2V4

[‡]Department of Materials Science and Engineering, Brockhouse Institute for Materials Research and Canadian Centre for Electron Microscopy, McMaster University, Hamilton, Ontario, Canada L8S 4L8

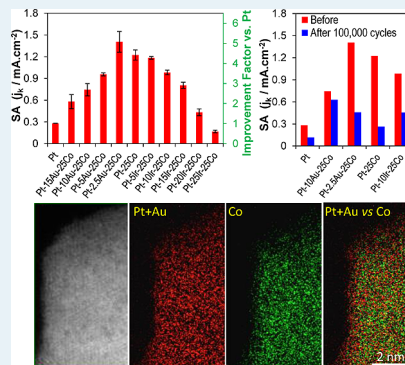
[§]Chemical & Biomolecular Engineering and Mechanical Engineering, Clarkson University, Potsdam, New York 13699, United States

^{||}Alberta Center for Surface Engineering and Science (ACSES), University of Alberta, Edmonton, Alberta, Canada T6G 2G6

Supporting Information

ABSTRACT: Here we investigate the oxygen reduction reaction electrocatalytic activity and the corrosion stability of several ternary Pt–Au–Co and Pt–Ir–Co alloys, with Pt–Au–Co having never been previously studied for ORR. The addition of Au fine tunes the lattice parameter and the surface electronic structure to enable activity and cycling stability that is unachievable in Pt–25 atom % Co (state-of-the-art binary baseline). The ternary alloys exhibit a volcano-type dependence of catalytic efficacy on the content of Au or Ir. Pt–2.5 atom % Au–25 atom % Co alloy shows a specific activity of 1.41 mA cm⁻² at 0.95 V, which is 16% and 404% higher than those of identically synthesized Pt–Co and pure Pt, respectively. This enhancement is promising in comparison to a range of previously published Pt “skeleton” and Pt “skin” alloys and is in fact the most optimum reported for a skeleton-type system. The catalysts exhibit dramatically improved corrosion stability with increasing levels of Au or Ir substitution, with the specific activity of all the ternary alloys being superior to that of Pt–Co after 100,000 potential cycles of 0.6–1.0 V. For instance, postcycled Pt–10 atom % Au–25 atom % Co shows a specific activity of 0.63 mA cm⁻², which is 140% higher than that of Pt–Co and 439% higher than that of Pt. HRTEM and XPS shows that Au alloying promotes the formation of an atomically thin Pt–Au-rich surface layer, which imparts kinetic stabilization against the dissolution of the less noble solute component.

KEYWORDS: PEM fuel cell, ORR, corrosion durability, Pt–Au–Co, Pt–Ir–Co, Pt–Co, thin film



INTRODUCTION

The development of proton exchange membrane fuel cells (PEMFCs) that are commercially more competitive demands more efficient electrocatalysts for the cathodic oxygen reduction reaction (ORR).¹ Despite progress in the development of non-noble electrocatalysts,^{2,3} platinum-based electrocatalysts continue to remain at the center of intense research.^{4–7} Many efforts have been directed toward enhancing the catalytic activity by developing advanced catalyst supports,^{8–11} by alloying Pt with transition metals (TM),^{12–18} or by catalyst surface design at the atomic level.^{19–21} The last includes well-known strategies such as dealloying of binary/ternary alloys,^{22–24} monolayer coating of Pt on a suitable metal substrate,^{25,26} and creation of the “Pt skin” electrocatalysts through thermal annealing of Pt alloys in a reduced environment.^{27–29}

The enhanced catalytic activities of the Pt-based alloy electrocatalysts and their derivatives, relative to pure Pt, originate from the compressed lattice^{30–32} and the modified electronic structures^{33,34} of Pt. Such a catalyst surface exhibits a slightly weaker binding than Pt to the intermediate oxygenated

spectator species (e.g., O^{*}, OH^{*}, and OOH^{*}) and thus an increasing number of active sites accessible to molecular oxygen.³³ However, it is important to note that further weakening of the oxygen binding induces a change in the rate-limiting step of the ORR, from OH^{*} + H⁺ + e[−] → H₂O(l) on the strong-binding side to O₂(g) + H⁺ + e[−] → OOH^{*} on the weak-binding side.^{12,34} This volcano-type dependence of catalytic efficacy on the surface oxygen binding energy is essentially another application of the traditional Sabatier principle,³⁵ which is typical for heterogeneous catalysis involving multiple reaction intermediates. The linearly scaling relations among the binding energies of O^{*}, OH^{*}, and OOH^{*} on the active sites of close-packed and stepped metal surfaces³⁶ make the oxygen binding energy a determinant parameter for ORR activity on Pt-based electrocatalyst surfaces.³³ Previous studies suggest that a surface which binds O^{*} 0–0.4 eV more weakly than Pt(111) should exhibit a better ORR activity than

Received: October 31, 2014

Revised: January 11, 2015

Pt, with the optimum being theoretically predicted at a binding energy of roughly 0.2 eV weaker than that of Pt.^{5,12}

Binary Pt-based electrocatalysts have been extensively studied for ORR. On the basis of the reported results, Pt–Co binary alloy catalysts, for example Pt₃Co, are highly active.^{37–40} However, the catalysts suffer from rapid catalytic decay due to the preferred leaching of the non-noble solute during electrode potential cycling in an acid medium.^{41–44} This is so far the greatest limitation for disordered Pt-based alloys with early or late transition metals.^{5–7,32} Platinum group metal (PGM) alloys have thus been proposed, aiming at improving the electrochemical stability. Considering the standard electrode potential, only Au and Ir (in addition to Pt) are thermodynamically stable in the bulk metallic form at potentials greater than 0.9 V. Unfortunately, binary Pt–PGM alloys are usually lacking in ORR catalytic activity. Pt/Au(111) has been reported to bind oxygen even more strongly than Pt(111), resulting in a sluggish ORR catalytic efficacy.⁴⁵ On the other hand, Pt–Ir and Pt–Ru binaries are known to bind oxygen too weakly, positioning on the far end of the other side of the volcano.⁴⁵ Guided by the reported properties of the individual binary systems, we hypothesize that fine tuning of ORR catalytic activity is possible by adding Au or Ir into a Pt–3d TM binary system. We understand that Au or Ir should be chosen on the basis of where the binary Pt–3d TM system is already positioned on the ORR volcano. For example, a binary system that is positioned on the weak-binding side should be tuned toward a stronger binding of oxygen, in order to reach the possible maximum on the ORR volcano. Such a hypothesis is consistent with the conclusion of recent theoretical modeling.⁴⁶

In the present work, we report a detailed study on the ORR electrocatalytic activities and the corrosion stabilities for Pt–Au–Co and Pt–Ir–Co alloys. By keeping the atomic ratio of PGM over Co fixed at 3:1, we systematically evaluated the ORR catalytic performance as a function of Au or Ir substitution, using binary Pt–25 atom % Co and pure Pt as the baseline. To the best of our knowledge, Pt–Au–Co alloy systems have never been studied for ORR. However, such ternary systems should be highly promising, given the increasing attention to ternary Pt–Au–X (X = Fe, Cu, Pd, Ni) alloy catalysts recently.^{47–51} It should be noted that Pt–Ir–Co alloy systems have already been reported,^{52–54} though the trend of catalytic activity has not been entirely established for such multimetallic systems. Herein, one of the main objectives of this study is to establish the trend of catalytic activity and corrosion stability for the ternary alloy catalysts. For that reason, we performed a systematic investigation on well-defined extended surfaces of thin-film model systems.

EXPERIMENTAL SECTION

Film Synthesis. The atomic ratio of platinum group metals (Pt + Au) or (Pt + Ir) versus Co was fixed at 3:1. As baselines, we synthesized and tested pure Pt and the known state-of-the-art binary alloy ORR catalyst Pt–25 atom % Co (i.e. Pt₃Co). For simplicity, we denote samples as Pt–xAu–25Co and Pt–xIr–25Co, which indicates a stoichiometry of (75 – x) atom % Pt–x atom % Au–25 atom % Co and (75 – x) atom % Pt–x atom % Ir–25 atom % Co. All depositions were conducted with the substrate temperature being maintained near ambient, resulting in a range of single-phase solid solution alloys. The thicknesses of all catalyst films were fixed at 20 nm, unless otherwise stated.

The catalyst thin films were magnetron-sputtered (AJA International, Orion) onto a mirror-polished glassy-carbon (GC) disk 11.32 mm in diameter, which was then directly employed as an electrode for the electrochemical measurements. The geometrical area of the active Pt surfaces was ~1 cm². Prior to catalyst deposition, the glassy-carbon surface was further treated with a mild Ar plasma procedure inside the sputtering chamber to promote better surface adhesion for the catalyst film. Deposition was performed in a sputter-up configuration with continuous substrate rotation. Argon gas with a purity of 99.999% was used at a working pressure of 5 × 10⁻³ mbar, with a maximum base vacuum of 3 × 10⁻⁸ mbar. The sputtering rate was accurately measured *in situ* using a crystal monitor at the substrate plane. Additional *ex situ* calibrations were performed to confirm the sputter rates employed and the resultant thicknesses. The deposition rate of Pt was kept at 1 Å s⁻¹. The deposition rates of Au, Ir, and Co were varied accordingly to adjust for different alloy stoichiometries.

Electrochemical Testing. Electrochemical measurements were carried out using a standard rotating-disk electrode (RDE) system (Princeton Applied Research Model 616), a Solartron 1470 multistat test station, and a three-electrode electrochemical cell. A helical Pt wire and Cl⁻ free Hg/Hg₂SO₄ with a taper joint were used as the counter and reference electrodes, respectively. Perchloric acid (HClO₄ optima grade, Fisher Scientific) diluted with Milli-Q water to 0.1 M was the electrolyte solution in all cases. All electrochemical measurements were carried out at room temperature using research-grade gases (99.999%, Praxair). The reported potentials are specified relative to the reversible hydrogen electrode (RHE) scale. Cyclic voltammetry (CV) was carried out in Ar-saturated electrolyte between 0 and 1.0 V with a scan rate of 100 mV s⁻¹. The electrochemical surface area (ECSA) of the catalyst was estimated by averaging the integral charges of the hydrogen adsorption and desorption areas of the CV profiles, including a correction for double-layer charging.⁵⁵ To avoid the underestimation of the ECSA owing to a possible suppression of hydrogen adsorption, the ECSA was confirmed by CO stripping.^{56,57} The authors of ref 56 were the first to demonstrate that a more reliable estimation of the electrochemically active surface area on Pt–Co is achieved using CO_{ads} stripping coulometry. Before CO stripping, the electrode was immersed in a CO-saturated electrolyte for 10 min. After that, the electrolyte was purged with Ar and the CO-stripping voltammogram was then recorded. Anodic linear sweep voltammetry (LSV) from 0.05 to 1.05 V was conducted in oxygen-saturated electrolyte to measure the ORR at different rotational speeds (100, 225, 400, 625, 900, 1225, 1600, 2025, and 2500 rpm) using a scan rate of 20 mV s⁻¹. The kinetic current was extracted from measured ORR polarization curve according to the Koutecky–Levich equation:

$$\begin{aligned} \frac{1}{I} &= \frac{1}{I_k} + \frac{1}{I_L} \\ &= \frac{1}{I_k} + \frac{1}{B\omega^{1/2}} \\ &= \frac{1}{I_k} + \frac{1}{0.62nFA_{\text{geo}}D^{2/3}\omega^{1/2}v^{-1/6}C_{\text{O}_2}} \end{aligned}$$

where I is the measured ORR current, I_k and I_L are the kinetic and the diffusion-limited currents, respectively, B is the Levich

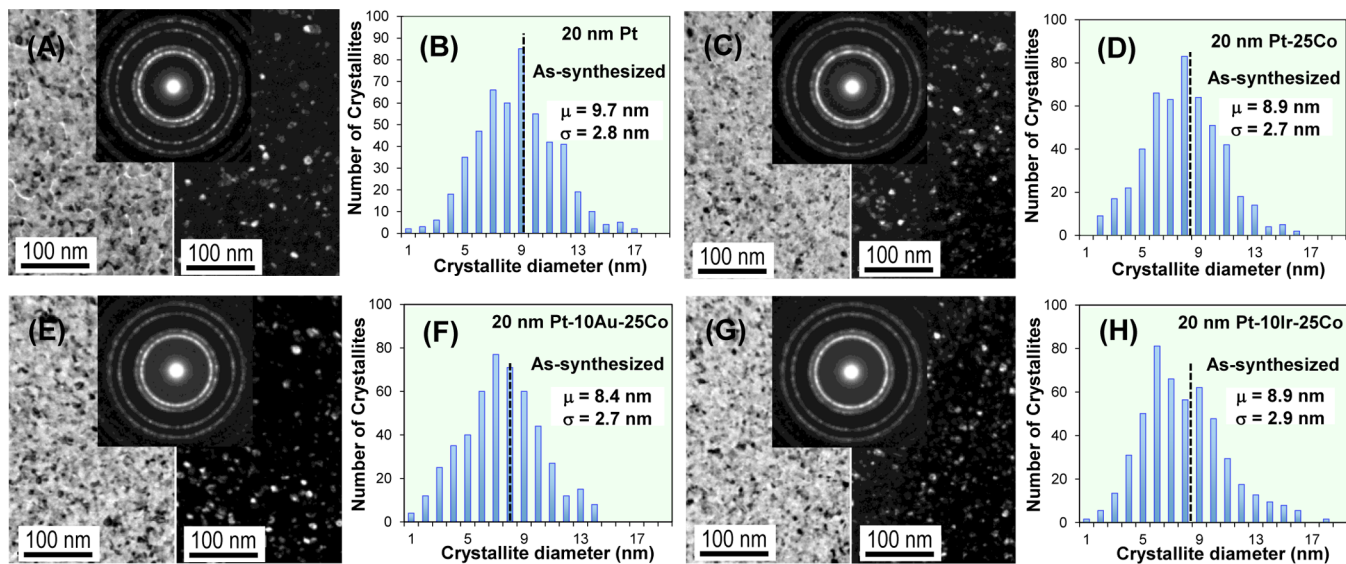


Figure 1. TEM bright field and dark field and selected area electron diffraction (SAED) micrographs and the corresponding catalyst crystallite size distributions of as-synthesized (A, B) pure Pt baseline, (C, D) Pt–25Co, (E, F) Pt–10Au–25Co, and (G, H) Pt–10Ir–25Co. Identical analyses for the other samples are presented in the Supporting Information. In each distribution the symbol μ denotes the mean crystallite diameter and σ denotes the associated standard deviation.

slope, F is the Faraday constant, n is the number of electrons transferred per O_2 molecule, D is the diffusion coefficient, C_{O_2} is the concentration of oxygen in the bulk solution, ω is the angular velocity, and ν is the kinematic viscosity of the solution. The electrocatalyst stability test involved 100000 potential cycles between 0.6 and 1.0 V using a sweep rate of 50 mV s⁻¹. CV and LSV were recorded after the 1st, 2nd, 5th, 10th, 50th, 100th, 200th, 300th, 400th, 500th, 5000th, 10000th, 20000th, 50000th, and 100000th cycles during the stability test. Prior to measuring the postcycling ECSA and ORR activities, the electrolyte was replaced with fresh solution. For the electrochemical impedance spectroscopy (EIS) measurements, we applied an alternating current in the frequency range from 20 kHz to 1 Hz with 10 mV amplitude at 0 V vs open circuit potential.

Microstructural Characterization. X-ray photoelectron spectroscopy (XPS) measurements were performed on an ULTRA (Kratos Analytical) spectrometer under ultrahigh vacuum (10^{-9} Torr) using monochromated Al K α radiation ($h\nu = 1486.6$ eV) operated at 210 W. All XPS spectra were calibrated using the universal hydrocarbon contamination C 1s peak at 284.8 eV. Angle-resolved XPS (ARXPS) analysis was conducted with an electron emission angle of 60° measured from the surface normal, denoted as ARXPS-60°. Such technique was used to enhance surface selectivity, sampling photoelectrons emitted from the very surface of catalyst films. While the ordinary XPS analysis, denoted as XPS-0°, collects photoelectrons from up to 5 nm depth of a metal surface, the ARXPS-60° analysis is expected to sample signals from a surface depth of only ~2 nm. We hereafter take the quantification results of XPS-0° analysis as the near-surface chemical composition, while taking the results of ARXPS-60° analysis as the surface chemical composition. We used CasaXPS software for the background removal, peak fitting, and calculation of the atomic concentration with the associated standard deviation. Background subtraction was done with a nonlinear Shirley-type model. Ultraviolet photoelectron spectroscopy (UPS) measurements were performed using a Kratos

Ultra spectrometer with He I light ($h\nu = 21.2$ eV). The analyzer pass energy was 5 eV, and the aperture was set at 110 μ m. X-ray diffraction (XRD) analysis was performed on a Bruker AXS diffractometer (Bruker Discover 8) using Cu K α radiation ($\lambda = 1.5406$ Å) that was monochromated using a single Gobel mirror. The diffractometer was equipped with a Histar general area two-dimensional detection system (GADDs) with a sample-detector distance of 15 cm. Given the same thicknesses for all catalyst films deposited on GC, the XRD patterns were calibrated using the universal GC(101) peak. Conventional bright field and dark field imaging and selected area electron diffraction (SAED) analysis were performed with a JEOL 2100 transmission electron microscope (TEM) operated at 200 kV accelerating voltage. Atomically resolved high angle annular dark field (HAADF) and electron energy loss spectroscopy (EELS) analyses were conducted on a FEI-Titan cubed TEM using scanning mode (STEM). The microscope was operated at 300 kV accelerating voltage and was equipped with two hexapole-design spherical aberration correctors of the probe and image forming lenses. TEM analysis of the as-synthesized microstructures were performed on catalyst films directly deposited onto the ultrathin carbon film on TEM grids. For postcycling analysis, the TEM specimens were mechanically removed from the electrodes and dry dispersed on the grids. The commercial software programs Crystal Maker and TEM diffraction ring profiler⁵⁸ were used to simulate electron diffraction patterns. On the basis of dark field TEM images, we determined the catalyst crystallite size distribution. For each sample, a total of 500 crystallites that displayed strong Bragg contrast were measured. Scanning electron microscopy (SEM) analysis was performed with a Hitachi S-4800 field emission SEM operated at 15 kV accelerating voltage.

RESULTS AND DISCUSSION

The 20 nm thick Pt–Au–Co and Pt–Ir–Co, binary Pt–Co, and pure Pt baseline catalyst films were deposited at ambient temperature onto mirror-polished glassy-carbon substrates. As shown by bright field transmission electron microscopy (TEM)

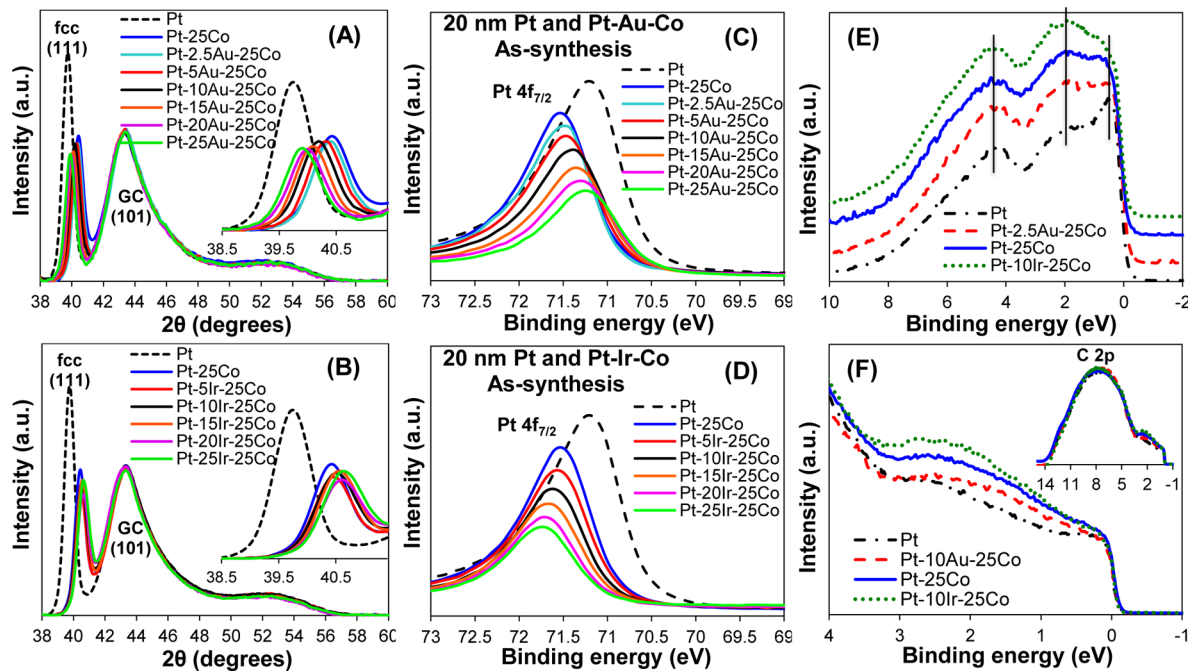


Figure 2. (A, B) XRD patterns and (C, D) Pt 4f_{7/2} XPS spectra of 20 nm Pt–Au–Co and Pt–Ir–Co alloy films, with Pt–25Co and pure Pt being included as the baselines. (E, F) Valence band spectra of selected samples, measured by (E) XPS and (F) UPS. As shown in the inset of (F), the UPS spectra have been normalized with respect to the C 2p peak at a binding energy of 8 eV.

Table 1. Results of XRD, EDS, XPS-0°, and Dark Field TEM Analysis of the As-Synthesized Catalyst Films, Summarizing the Measured Lattice Parameters, Bulk and Near-Surface Chemical Compositions, and Mean Crystallite Diameters^a

	X-ray 2θ fcc (111) (deg)	fcc lattice param (Å)	EDS bulk composition (atom %)			XPS-0° near-surface composition (atom %)			TEM crystallite diameter distribn (nm)
			Pt	Au/Ir	Co	Pt	Au/Ir	Co	
Pt	39.75	3.924	100			100			9.7 ± 2.8
Pt–25Au–25Co	39.91	3.909	54.0	22.5	23.5	49.4	28.6	22.0	8.6 ± 2.6
Pt–20Au–25Co	39.98	3.902	57.7	19.0	23.3	55.2	22.6	22.2	8.7 ± 2.7
Pt–15Au–25Co	40.09	3.892	59.8	15.3	24.9	59.9	17.0	23.1	8.1 ± 2.2
Pt–10Au–25Co	40.19	3.882	65.9	10.2	23.9	65.2	11.0	23.8	8.4 ± 2.7
Pt–5Au–25Co	40.32	3.870	70.4	5.9	23.7	70.4	5.5	24.1	7.8 ± 2.4
Pt–2.5Au–25Co	40.40	3.863	71.8	3.6	24.6	73.1	2.5	24.4	7.8 ± 2.4
Pt–25Co	40.43	3.860	74.3		25.7	73.9		26.1	8.9 ± 2.7
Pt–5Ir–25Co	40.47	3.857	69.9	5.1	25.0	69.2	5.4	25.4	8.4 ± 2.7
Pt–10Ir–25Co	40.52	3.852	63.6	12.1	24.3	64.9	10.9	24.2	8.9 ± 2.9
Pt–15Ir–25Co	40.57	3.848	58.8	16.1	25.1	59.6	16.5	23.9	8.8 ± 2.3
Pt–20Ir–25Co	40.61	3.844	56.8	19.3	23.9	53.7	20.6	25.7	8.5 ± 2.2
Pt–25Ir–25Co	40.64	3.841	51.6	24.9	23.5	49.2	26.2	24.6	8.3 ± 2.1

^aThe associated error bars for EDS and XPS analysis are summarized in Tables S1 and S2, respectively, in the Supporting Information.

analysis (Figure 1 and Figure S1 (Supporting Information)), all of the as-synthesized films are continuous. This geometric feature of the electrocatalysts is important for carrying out a systematic evaluation of ORR activities as a function of composition. Schneider et al. demonstrated that the separation and the size of Pt nanoparticles on a planar glassy-carbon electrode will have a pronounced effect on the hydrogen peroxide yield.⁵⁹ Nesselberger et al. also demonstrated that the catalyst interparticle distance will decisively influence the measured catalytic activity.⁶⁰ It is well documented that the catalyst particle/crystallite size has a profound impact on the ORR activity.⁶¹ Thus, if our films were a series of dewetted particles of differing dimensions and spacings, the interpretation of their activity versus composition would be less

straightforward. By sputtering at room temperature using almost identical deposition rates, i.e. ensuring analogous kinetic energies of the sputtering fluxes, very similar mean crystallite sizes of ~8 nm have been achieved for all systems, as demonstrated by extensive dark field TEM analysis along with statistically determined crystallite size distribution (Figure 1 and Figure S1). The aforementioned experimental designs provided a platform of model study to establish the trend of catalytic performance as a function of alloy composition.

Typical selected area electron diffraction (SAED) patterns are shown in the insets of Figure 1. All catalyst films are random solid solutions with face-centered cubic (fcc) crystal structures (the complete SAED diffraction analysis are detailed in Figures S1 and S2 in the Supporting Information). As shown by the

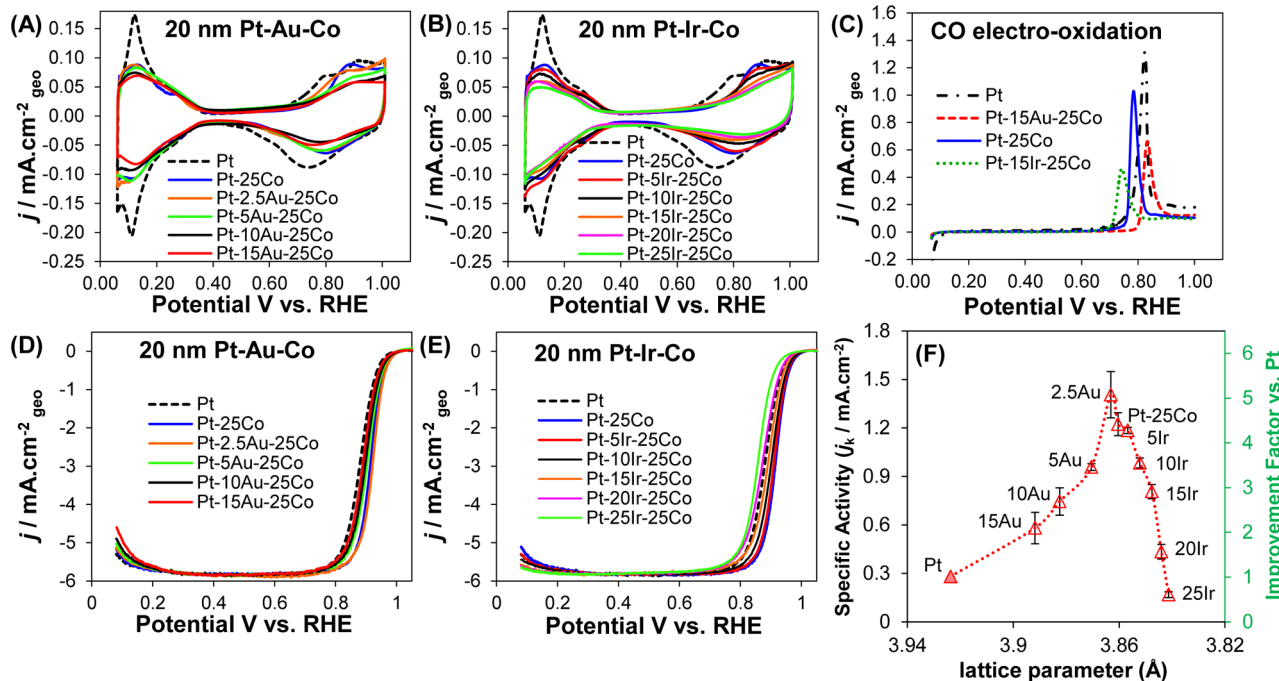


Figure 3. (A, B) Cyclic voltammetry (CV) of Pt–Au–Co, Pt–Ir–Co, Pt–25Co and pure Pt in argon-saturated 0.1 M HClO_4 solution using a scan rate of 100 mV s^{-1} . (C) CO stripping curves for selected samples. (D, E) Master plots comparing the iR -corrected ORR polarization curves at 1600 rpm in oxygen-saturated electrolyte using a scan rate of 20 mV s^{-1} . All electrochemical tests were conducted at room temperature. (F) Specific activities measured at 0.95 V versus RHE. The improvement factors relative to the pure Pt baseline are plotted as a function of lattice parameters that were experimentally determined by XRD analysis. The triangular data points represent the experimental results, averaged from two independent measurements. The error bars show the deviation from the mean.

results of the X-ray diffraction (XRD) analysis (Figure 2A,B), the fcc (111) peak of Pt–Au–Co alloys shifted toward lower angles with increasing Au content. This observation is in accordance with Vegard’s law, since Au substitution with a crystal lattice parameter larger than that of Pt will gradually compensate the lattice compression, as induced by alloying with Co. Meanwhile, the (111) peak of Pt–Ir–Co alloys remains essentially unchanged. This is as expected, given the similar lattice parameters between the Pt and Ir crystal structures. For each sample, we have used energy-dispersive X-ray spectroscopy (EDS) to confirm the bulk composition. In parallel, we carried out X-ray photoelectron spectroscopy (XPS- 0°) analysis to examine the near-surface composition. It is noted that the alloy composition near the surface starts to deviate from the bulk value with increasing Au content. There, the relatively higher concentration of Au on the surface indicates preferred segregation. This could be explained by the differences in surface segregation energies of Au, Pt, and Co.^{47,62} The results of the microstructural characterizations for the initial microstructure of all samples are summarized in Table 1.

Figure 2C,D shows the Pt $4f_{7/2}$ X-ray photoelectron spectroscopy (XPS) spectra of the as-synthesized Pt–Au–Co and Pt–Ir–Co alloy films, respectively. The XPS spectra of the Pt–25Co and pure Pt baselines are included for reference. There is a clear shift in the Pt $4f_{7/2}$ core level (CL) as a function of Au or Ir alloying compositions. While the surface CL of Pt–Au–Co alloys shifts to lower binding energies in comparison to Pt–25Co, the surface CL of Pt–Ir–Co alloys shifts to higher binding energies. The shift in CL is associated with a shift in the center of gravity of the d bands.^{63,64} It has been previously shown that a CL shift to a higher binding energy indicates a

downshift in d band center with respect to the Fermi level,^{65,66} and thus vice versa for a CL shift to a lower binding energy. Additionally, we carried out XPS and ultraviolet photoelectron spectroscopy (UPS) analysis to directly probe the changes in valence band for selected samples. The results, as shown in Figure 2E,F, respectively, support our arguments based on CL shift. As Pt d band character dominates the band structures of alloy surfaces, it may be seen that the 5d band center of Pt is shifting downward in the following order: Pt > Pt–Au–Co > Pt–25Co > Pt–Ir–Co. Considering the strong correlation between the d band center of a given catalyst surface and the oxygen binding energy,³³ we anticipate a predictable variation in the ORR activity of the alloys with the level of Au or Ir substitution for Pt.

Cyclic voltammetry (CV) and rotating-disk-electrode (RDE) linear sweep voltammetry (LSV) were used to investigate the electrochemical adsorption and catalytic properties of the catalyst electrodes. Figure 3A,B compares the CV profiles of Pt–Au–Co and Pt–Ir–Co, respectively. These CV tests were performed in argon-saturated 0.1 M HClO_4 solution using a scan rate of 100 mV s^{-1} . Close inspection of the CV profiles reveals that, by varying the substitution level of Au or Ir, the electrochemical adsorption properties of the resulting surfaces are significantly altered. Using binary Pt–25Co and pure Pt as the references, the reduction of O-containing species on Pt–Au–Co surfaces is observed to fall between the two. We are careful not to state with certainty what the exact adsorbed species is, OH^* or O^* , as this has not been fully resolved in the literature and most likely depends at least in part on the catalyst geometry. For example, results presented in ref 67 point to the stable surface compound being PtO rather than PtOH . However, OH^* could exist as a chemisorbed intermediate,

particularly on Pt(111), which subsequently oxidizes to O^{*}. With increasing levels of Au substitution, the reduction peak gradually shifts toward that of pure Pt: i.e., to a more negative potential. This observation confirms stronger oxygen binding on Pt–Au–Co surfaces relative to Pt–25Co, which can be attributed to the expanding lattice and the upward shift of the d band center toward the Fermi level. For Pt–Ir–Co alloys, there is an opposite trend: with increasing levels of Ir substitution they exhibit progressively more positive shifts in the reduction peak. This indicates further weakening of the electrochemically adsorbed O-containing species on Pt–Ir–Co in comparison to Pt–25Co.

Figure 3C shows the CO stripping curves for Pt–10Au–25Co, Pt–10Ir–25Co, Pt–25Co, and pure Pt. As CO- and O-containing species are competing for the same Pt adsorption sites, the trend observed for CO electro-oxidation is consistent with the above trend for the reduction of surface O-containing species. While the electro-oxidation of adsorbed CO proceeds at lower potentials on the surfaces of Pt–10Ir–25Co and other Pt–Ir–Co alloys in comparison to binary Pt–25Co, higher potentials are required to strip the CO from the surfaces of Pt–10Au–25Co and other Pt–Au–Co alloys. Our results of CO stripping and XPS analysis demonstrate a correlation between the changes in CO chemisorption energy and the relative shifts in surface CL binding energy. These trends agree well with an earlier study of CO thermal adsorption on Pd, Ni, and Cu overlayers on various supports, where the CO desorption temperature was found to be lower with a relative shift in surface CL to higher binding energies.⁶⁸ To summarize the effects of Au or Ir substitution on chemical interactions of alloy catalyst surfaces with O-containing species or CO: adding Au stabilizes the adsorbates, and adding Ir destabilizes the adsorbates.

We estimated the electrochemical surface area (ECSA) by both integral charges of underpotentially deposited hydrogen (H_{upd}) and CO electro-oxidation. As shown in Figure S3 in the Supporting Information, the ratio between the two integral charges remains close to 1 for all investigated samples. This rules out the formation of a thermally segregated Pt-skin structure with its characteristic ratio of close to 1.5 and agrees with the homogeneous structure expected from near-ambient substrate temperatures during deposition. During the initial potential cycling, a leached-type “Pt skeleton” will most likely develop on the surface of a random solid solution alloy.⁶⁹ It has been reported that the nonannealed alloy surface does not show a discrepancy between the ECSA based on H_{upd} and CO stripping,^{12,70} and therefore the surface area estimation based on the integral charge of H_{upd} is reasonable. Table 2 provides ECSA estimates based on H_{upd} .

Figure S4 in the Supporting Information presents the complete set of ORR polarization curves for all investigated electrocatalysts, tested between 100 and 2500 rpm at room temperature. These LSV measurements were conducted in oxygen-saturated 0.1 M HClO₄ solution using a scan rate of 20 mV s⁻¹. The RDE data were analyzed with the Koutecky–Levich (K-L) approach to extract the kinetic currents from the polarization curves. The number of electrons transferred (n) per O₂ molecule calculated from the slope of the K-L plot supports the complete four-electron reduction of O₂ to H₂O.

Figure 3D,E provides the master plots of iR -corrected ORR polarization curves at 1600 rpm, comparing the initial catalytic efficacies of different electrocatalysts. The overall resistance of the electrochemical cell was obtained from the real component

Table 2. Initial Electrochemical Surface Area (ECSA) and ORR Half-Wave Potentials ($E_{1/2}$) for Pt–Au–Co, Pt–Ir–Co, Pt–25Co, and Pure Pt Electrocatalysts

	ECSA (cm ²)	ECSA (m ² g _{Pt} ⁻¹)	$E_{1/2}$ (V)
Pt	1.03	2.57	0.880
Pt–15Au–25Co	0.61	2.43	0.884
Pt–10Au–25Co	0.66	2.41	0.898
Pt–5Au–25Co	0.71	2.37	0.904
Pt–2.5Au–25Co	0.73	2.36	0.922
Pt–25Co	0.74	2.30	0.915
Pt–5Ir–25Co	0.66	2.20	0.910
Pt–10Ir–25Co	0.62	2.21	0.901
Pt–15Ir–25Co	0.52	2.00	0.891
Pt–20Ir–25Co	0.51	2.13	0.872
Pt–25Ir–25Co	0.50	2.28	0.857

value of the impedance at the minimum of the Nyquist plot. The results of electrochemical impedance spectroscopy (EIS) for all catalyst electrodes are shown in Figure S5 in the Supporting Information. The investigated catalyst electrodes show similar resistances of $\sim 12 \Omega$. This result demonstrates another advantageous consistency of using a model system of thin film catalysts. As shown in Figure 3D, the polarization curves of Pt–Au–Co alloys show first an increase in half-wave potential ($E_{1/2}$) from binary Pt–25Co to Pt–2.5Au–25Co and then a quick decrease in $E_{1/2}$ with further increasing levels of Au substitution. As shown in Figure 3E, the polarization curves of Pt–Ir–Co alloys show a monotonic decrease in $E_{1/2}$ with increasing Ir substitution. Table 2 also provides the list of $E_{1/2}$ values for all investigated samples.

The ORR specific activities, which represent the intrinsic efficacy of the electrocatalysts, were calculated through normalization by ECSA. Figure 3F plots the initial specific activities, measured at 0.95 V vs RHE, as a function of the measured bulk lattice constants. For initial catalytic performance, the bulk lattice parameter of a homogeneous solid solution represents a reasonable estimate of the surface lattice constant. The volcano plot of the catalytic activities versus lattice constants is clearly uneven across the composition range. This suggests that the observed trend of ORR activities versus Au or Ir substitution level is not solely due to the change in lattice. Rather, it is caused by a combination of geometric and electronic effects. This argument is in line with the general understanding of Pt alloy catalysts, where the strain and the ligand effects are usually inseparable.¹³ We also point out that the lattice parameter of the as-synthesized surfaces will be commensurate with its bulk composition as long as major segregation does not occur. Conversely, in segregated specimens (e.g., due to prolonged or high temperature aging) the lattice parameter of the surface may be in fact incommensurate with its bulk composition. This would result in epitaxial-type strain and a deviation of the catalytic activity from expected “bulk” values.

The ultimate outcome of the changes in the lattice parameter and the electronic structure is a modification of the oxygen binding energy on a catalyst surface: i.e., its catalytic activity.^{13,33,45} On the basis of the results of XRD and XPS analysis, combined with the measured properties of electrochemical adsorption, we herein describe the volcano of ORR activities as a function of oxygen binding energies. From high to low level of Au substitution (sample Pt–15Au–25Co to sample Pt–2.5Au–25Co), the Pt–Au–Co alloy surfaces exhibit

Table 3. Comparison of the Achieved Improvement Factors of Our Best-Performing Pt–Au–Co Alloys with Those of Previously Reported State-of-the-Art ORR Electrocatalysts

electrocatalyst	cat. type ^a	surface type	improvement factor	SA (mA cm ⁻²)	measd @ (V vs RHE)	T (°C)
PtNi ²⁸	TF	Pt skin	13.2	5.6	0.95	60
Pt _{2–3L} /intermetallic Pt ₃ Co ³⁹	NP	Pt skin/core–shell	11.2	1.25	0.90	room temp
Pt ₃ Ni(111) ⁷¹	bulk SC	Pt skin	10.0	18	0.90	60
Cu/Pt(111) NSA ³⁴	AL on Pt SC	NSA	8.0	10.1	0.90	60
Pt ₃ Y ¹³	bulk PC	Pt skin	6.0	11	0.90	room temp
Pt–2.5Au–25Co (this study)	TF	Pt skeleton	5.0	1.41	0.95	room temp
Pt ₄₅ Ni ₅₅ –Pt ₅₅ Ni ₄₅ ¹⁵	TF	Pt skeleton	4.7	2.8	0.90	room temp
Pt ₃ (CoNi) ¹²	TF	Pt skin	3.9	1.75	0.95	60
PtCu dealloyed ³⁰	NP	core–shell	3.8	0.75	0.90	room temp
PtNi ²⁸	TF	Pt skeleton	3.4	1.5	0.95	60
Pt ₃ (FeNi) ₁ ¹²	TF	Pt skin	3.3	1.47	0.95	60
Pt ₃ Co ³³	TF	Pt skin	3	4.3	0.90	60
Pt–10Au–25Co (this study)	TF	Pt skeleton	2.7	0.75	0.95	room temp
Pt _{ML} /Pd ₀ Au ₁ ⁷⁶	NP	Pt monolayer	2.7	0.38	0.90	80
Pt ₃ Fe/Au(111) ⁴⁷	TF	Pt skeleton/core–shell	2.6	6.7	0.90	60
Pt ₃ Fe ³³	TF	Pt skin	2.6	3.75	0.90	60
Pt ₃ (CoNi) ₁ ¹²	TF	Pt skeleton	2.5	1.12	0.95	60
Pt ₃ (FeCo) ₁ ¹²	TF	Pt skin	2.4	1.1	0.95	60
Pt ₃ (FeNi) ₁ ¹²	TF	Pt skeleton	2.3	1.03	0.95	60
Pt ₃ Ni ³³	TF	Pt–skin	2.25	3.25	0.90	60
Pt ₃ Co ⁶⁹	TF	Pt skeleton	2	2.8	0.90	60
Pt ₃ (FeCo) ₁ ¹²	TF	Pt skeleton	1.9	0.85	0.95	60
Pt ₃ Ni ⁶⁹	TF	Pt skeleton	1.8	2.7	0.90	60
Pt ₃ V ³³	TF	Pt skin	1.7	2.5	0.90	60
Pt ₃ Fe ⁶⁹	TF	Pt skeleton	1.63	2.25	0.90	60
Pt _{2–3L} /Pd ²⁰	NP	core–shell	1.6	0.48	0.90	room temp
Pt ₃ Ti ³³	TF	Pt skin	1.4	2	0.90	60
Pt _{ML} /Pd(111) ⁴⁵	ML on SC	Pt monolayer	1.34	16.5	0.80	room temp
Pt ₃ V ⁶⁹	TF	Pt skeleton	1.3	1.85	0.90	60
Pt ₃ Ti ⁶⁹	TF	Pt skeleton	1.05	1.5	0.90	60
Pt _{ML} /Au(111) ⁴⁵	ML on SC	Pt monolayer	0.85	10.4	0.80	room temp
Pt _{ML} /Rh(111) ⁴⁵	ML on SC	Pt monolayer	0.55	6.8	0.80	room temp
Pt ₃ Sc ¹³	bulk PC	Pt skin	0.5	2.38	0.90	room temp
Pt _{ML} /Ir(111) ⁴⁵	ML on SC	Pt monolayer	0.45	5.5	0.80	room temp
Pt _{ML} /Ru(111) ⁴⁵	ML on SC	Pt monolayer	0.11	1.4	0.80	room temp

^aAbbreviations: TF, thin film; NP, nanoparticle; NSA, near-surface alloy; AL, atomic layer; ML, monolayer; SC, single crystal; PC, polycrystalline.

increasing ORR catalytic activities with gradually decreasing oxygen binding energies relative to pure Pt. This is indicative of lower activation barriers for electroreduction of OH* and thus higher availability of active surface sites that are accessible to oxygen. For an Au substitution level of 10 atom %, the Pt–10Au–25Co alloy shows a specific activity of 0.75 mA cm⁻² at 0.95 V. We employ a figure of merit termed specific activity improvement factor (IF). IF is defined as the ratio of specific activity of the alloy catalyst divided by that of an identically synthesized pure Pt baseline, measured at the same voltage. For Pt–10Au–25Co, the obtained catalytic enhancement represents an improvement factor of 2.7 compared to the identically synthesized Pt baseline. For Au substitution level of 2.5 at. %, we have achieved fine-tuning of the ORR electrocatalytic activity toward the volcano peak by discovering a Pt–Au–Co alloy surface that binds oxygen weaker than Pt but slightly stronger than Pt–25Co. The Pt–2.5Au–25Co shows an ORR specific activity of 1.41 mA cm⁻² at 0.95 V, even higher than that of the state-of-the-art binary Pt–25Co. This represents an improvement factor of 5 compared to the Pt baseline. The result makes good sense, considering that binary Pt–25Co alloy surface was previously found to position just to the weak-

binding side of ORR volcano.^{5,12} Alternatively, Ir substitution to binary Pt–25Co is not effective for enhancing the ORR catalytic activity. From low to high level of Ir substitution (sample Pt–5Ir–25Co to sample Pt–25Ir–25Co), Pt–Ir–Co alloy surfaces exhibit further weakening in oxygen binding in comparison to binary Pt–25Co. This induces a change in the rate-limiting step, with the ORR being limited by an increased activation barrier for oxygen dissociation or the hydrogenation of oxygen.

Table 3 compares some of our best-performing Pt–Au–Co alloy electrocatalysts with the state-of-the-art species previously reported in the scientific literature. We target a comparison to the results reported for a range of alloy and bilayer systems, including works based on thin-film polycrystalline surfaces, single-crystal surfaces, monolayer Pt deposited on single-crystal substrates, and also several nanoparticulate materials. In these studies the authors avoided using commercial Pt/C as a baseline, presumably because commercial Pt/C catalysts usually demonstrate specific activity significantly lower than that of the extended Pt surfaces.⁷¹ We rank the performances of alloy catalysts on the basis of their IF, which was obtained directly from the published data. In Table 3, the reported specific

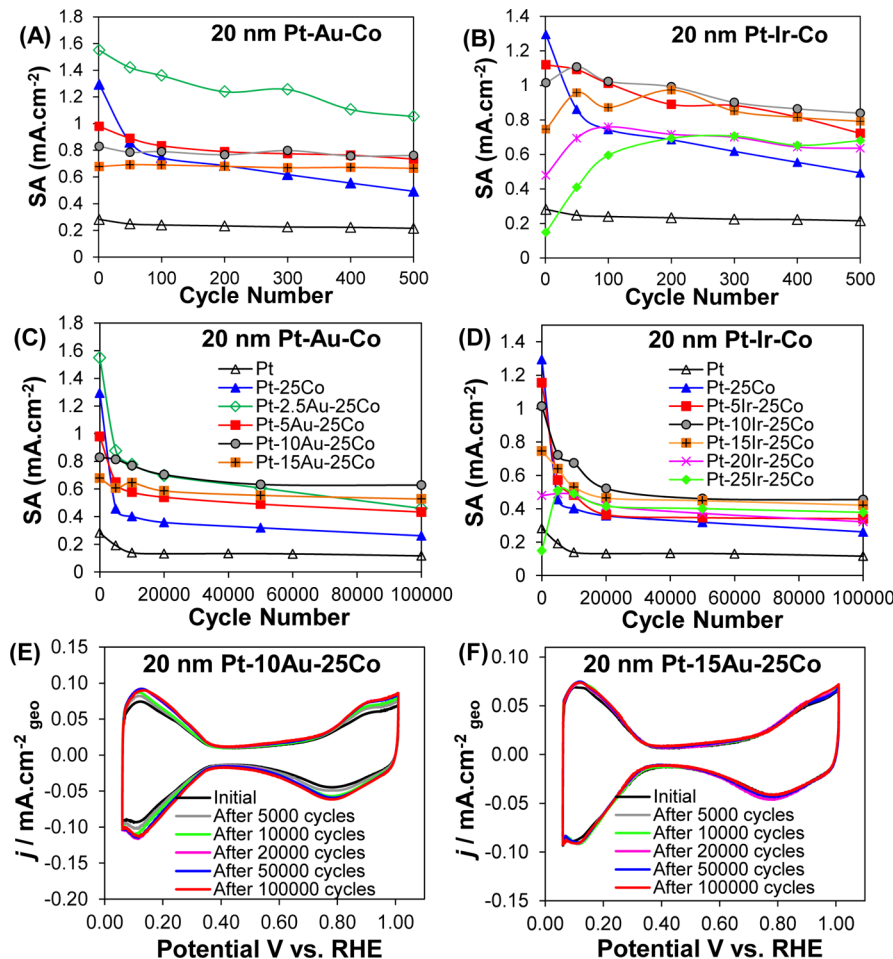


Figure 4. Catalyst stability test with 100000 potential cycles between 0.6 and 1.0 V at a sweep rate of 50 mV s⁻¹ at room temperature. The ORR-specific activities (SA) at 0.95 V versus RHE for Pt–Au–Co, Pt–Ir–Co, Pt–25Co, and pure Pt are plotted as a function of potential cycle number. (A, B) SA during the initial 500 cycles. (C, D) SA in the course of 100000 cycles. (E, F) CV of (E) Pt–10Au–25Co and (F) Pt–15Au–25Co during cycling, with the rest of the samples being shown in Figure S6 in the Supporting Information.

activity, the voltage, and the temperature at which the activity was measured are included for reference only. Of course, activity values may not be directly compared if they are measured at different potentials/temperatures. It is noteworthy that our Pt–2.5Au–25Co alloy in fact exhibits the highest IF (a factor of 5) ever reported for a skeleton-type Pt alloy electrocatalyst. For Pt–10Au–25Co, the obtained catalytic enhancement, an IF of 2.7, is still highly promising. The few materials from the literature with higher IF values than 5 are either Pt–skin systems or in one case a near-surface alloy, both of which are expected to possess greatly enhanced activity at the expense of long-term cycling durability. For instance, authors recently reported a significant evolution of the surface structure of a monolayer Pt skin on Pt–Co alloy catalyst just due to an acid treatment (i.e., without voltage cycling).⁷² Specifically an initially well-defined Pt–skin structure upon exposure to 1 M H₂SO₄ solution has turned into a Pt–skeleton structure that is made of two to three Pt overlayers surrounding a Pt–Co alloy core, with the global Co content of the catalyst being reduced from 27 to 17 atom %.

The durability of the electrocatalysts was evaluated by 100000 potential cycles between 0.6 and 1.0 V, at room temperature, using a sweep rate of 50 mV s⁻¹. For all investigated electrocatalysts, the ORR polarization curves and the CV profiles measured at different stages of stability tests are

detailed in Figure S6 in the Supporting Information. Figure 4A–D depicts the results of stability tests for Pt–Au–Co, Pt–Ir–Co, binary Pt–25Co, and pure Pt, plotting the ORR specific activities at 0.95 V as a function of potential cycle number. The results during the initial 500 cycles are detailed in Figure 4A,B. Interestingly, while Pt–Au–Co and pure Pt show monotonic degradation in ORR specific activities during the initial 500 cycles, Pt–Ir–Co and Pt–25Co alloys first show an increase in ORR activity before their activities start to degrade with higher cycle numbers. We term this temporary increase as an “activation period”. The length of this activation period varies with the sample compositions. While for Pt–25Co the activation is 2 cycles, the activation period of Pt–Ir–Co lasts for more cycles with increasing Ir content. For Pt–5Ir–25Co, Pt–10Ir–25Co, Pt–15Ir–25Co, and Pt–25Ir–25Co, the activation period lasts for ~10, 50, 100, 150, and as long as 300 cycles, respectively. We hypothesize that this ORR activation behavior for Pt–Ir–Co and Pt–25Co systems is related to the early-stage Co dissolution that actually results in favorable changes in lattice and electronic structures of the alloy surface. As discussed for Figure 3F, the Pt–Ir–Co alloys with high Ir content should bind oxygen too weakly, exhibiting sluggish initial ORR activities. With progressive Co dissolution, the partial relaxation of surface lattice strain and electronic effect would first initiate an increase in ORR activity, on moving

from the right side of the activity volcano toward the peak. We argue that our hypothesis may indeed be the case, though a more complex early stage activation behavior may be associated with Pt–Ir–Co systems.

Figure 4C,D shows the results over the course of 100000 potential cycles. For Pt–25Co, such extended stability tests result in a substantial degradation in ORR activity, which happens particularly quickly at the early stage of potential cycles. Although the specific activity of Pt–25Co was initially as high as 1.294 mA cm^{-2} at 0.95 V, it is degraded by 43% after 100 cycles, by 62% after 500 cycles, and by nearly 80% after 100000 potential cycles. For Pt–Co binary catalyst, Co dissolution is certainly the key factor for the decrease in the ORR specific activity due to the loss of geometric and electronic effects. The specific activity of the ternary alloys shows progressively less cycling degradation with increasing levels of Au/Ir substitution. After 100000 cycles the specific activity degradations in Pt–2.5Au–25Co, Pt–5Au–25Co, Pt–10Au–25Co, and Pt–15Au–25Co are 70%, 56%, 25% and 22%, respectively. For Pt–5Ir–25Co, Pt–10Ir–25Co, Pt–15Ir–25Co, and Pt–20Ir–25Co these values are 71%, 55%, 43%, and 33%, respectively. All of the Pt–Au–Co and Pt–Ir–Co alloys possess higher activities than Pt–Co after 100000 cycles. Here, we highlight the catalytic stability for Pt–10Au–25Co alloy. Despite the lower initial ORR activity, its specific activity after 100000 cycles is actually 2.4 times higher than that of Pt–25Co. As will be demonstrated later, an important benefit of Au substitution is the reduction in the rate of Co dissolution. We argue that this is achieved through the stable presence of Au at the catalyst surface, which in turn reduces the leaching out of the underlying Co atoms.

Figure S7 in the Supporting Information shows the evolution of ECSA for Pt–Au–Co, Pt–Ir–Co, Pt–25Co, and pure Pt over the course of 100000 potential cycles. Unlike other supported electrocatalyst particulates, continuous catalyst thin films with sufficient thickness do not show loss in ECSA, at least for a certain range of cycling number. Instead, the ECSA values of all investigated catalyst films actually increase over cycling, with higher gains in ECSA for samples having more degradation in activity. For the alloy catalysts, the dealloying of the Co solute component is also the key factor for the increase in ECSA. The preferred leaching of Co atoms, which are known for having no affinity to H, will create a catalyst surface that is atomically corrugated. The dealloyed surfaces may also contain higher fractions of H-adsorbing elements in comparison to their original state. Consequently, any loss in real surface area due to Pt dissolution could be covered by an increasing H adsorption on surfaces that are depleted of the solute component. The ECSA values of Pt-based alloy catalysts gradually increase to a stage where a steady-state value is achieved. This implies that the dealloyed Pt-rich or PGM-rich catalyst surface has rearranged to form a continuous overlayer, which should provide kinetic stability against further dissolution of the less noble solute component.^{73,74} Figure 4E,F shows the CV profiles of Pt–10Au–25Co and Pt–15Au–25Co, respectively, in the course of 100000 potential cycles. For the Pt–Au–Co species that have sufficient levels of Au substitution (≥ 10 atom %), their essentially unchanged CV and minimal changes in activity and ECSA during cycling signal a tremendously enhanced resistance to degradation.

For the cycling behaviors of pure Pt baseline catalyst film, we wish to point out a different explanation, which may also be applicable to other polycrystalline alloy films that were initially

continuous. Driven by higher free energy, low-coordinated atoms at grain boundaries are more prone to oxidation and dissolution. As shown by the high-magnification scanning electron microscopy (SEM) images of 20 nm Pt film after cycling (see Figure S8 in the Supporting Information), rapid dissolution at grain boundaries has turned the continuous polycrystalline film into Pt crystallites that are isolated or partially interconnected. This process increases the film surface roughness, exposing more electrochemically active surface to the electrolyte. The process that turns a continuous Pt film into isolated crystallites also changes the proportion of the Pt crystal facets that are exposed to the electrolyte (see Figure S9 in the Supporting Information). It is well documented that the ORR activities on the low-index Pt single-crystal surfaces in perchloric acid increase in the order $\text{Pt}(100) \ll \text{Pt}(111) < \text{Pt}(110)$, being attributed to the structure-sensitive adsorption of reaction intermediates on different facets.^{7,75} A decreasing ratio of Pt(110) to Pt(100) over cycling would explain the decaying ORR specific activity for pure Pt.

Figure 5 compares the surface ~ 2 nm sampling depth (ARXPS-60°) versus the near-surface ~ 5 nm sampling depth

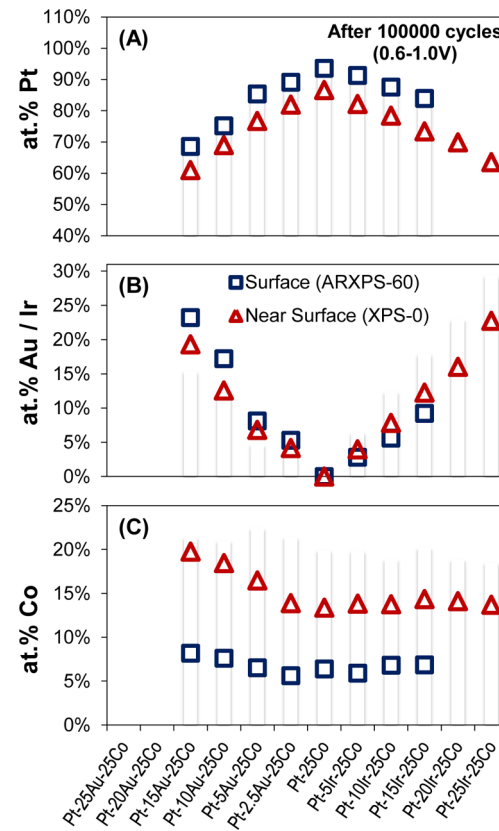


Figure 5. Comparisons of surface (penetration ~ 2 nm) and near-surface (penetration ~ 5 nm) chemical compositions for (A) Pt, (B) Au or Ir, and (C) Co, respectively, after 100000 potential cycles between 0.6 and 1.0 V.

(XPS-0°) chemical compositions of the electrocatalysts after 100000 potential cycles. For Pt–Au–Co alloys, with increasing Au additions the near-surface Co content is progressively stabilized relative to Pt–Ir–Co and to Pt–Co alloys. This indicates that the initial structure of Pt–Au–Co alloys is better maintained in comparison to the other systems. The Pt–Au-rich surface layer acts as a protective layer for the alloy structure

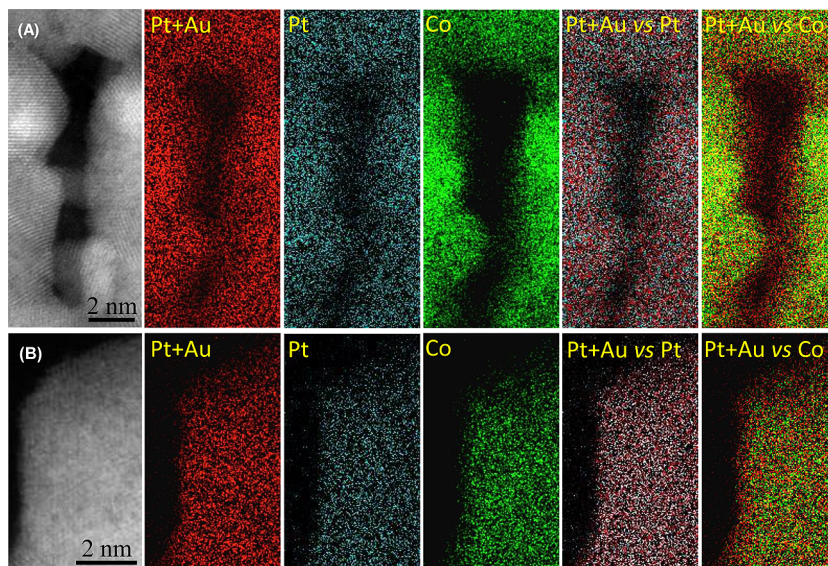


Figure 6. High-resolution HAADF micrographs and EELS elemental maps of Pt+Au, Pt, and Co for 5 nm Pt-10Au-25Co alloy film (A) before and (B) after 5000 potential cycles between 0.6 and 1.0 V.

underneath, resulting in an enhanced preservation of the useful strain and electronic effects from the subsurface Co solute.

The catalyst surface structure of Pt-10Au-25Co alloy was further characterized using HRTEM HAADF and EELS elemental mapping, conducted on a thinner 5 nm sample. The core-loss edges of Pt M_{4,5}, Au M_{4,5} and Co L_{2,3} are at 2120, 2206, and 779 eV, respectively. Given the difficulty of deconvoluting Pt and Au signals from the EELS (as detailed in the Supporting Information and Figure S10), we acquired Pt+Au combined, Pt, and Co elemental maps. As may be seen in the map of the as-synthesized alloy (Figure 6A), the material is overall quite homogeneous on the atomic scale. However, there does appear to be a subnanometer thick Pt-Au-rich surface layer in this specimen. On the basis of the aberration-corrected HR EELS elemental maps, the Pt-Au-rich surface layer is about 0.5 nm, which corresponds to two to three atomic layers. Such fine segregation would be driven by the differences in surface segregation energies of Au, Pt, and Co, with the diffusion distances being small enough for it to occur even at ambient temperature. As shown in Figure 6B, a similar scale Pt-Au-rich surface layer also exists after 5000 potential cycles between 0.6 and 1.0 V. Figure S11 in the Supporting Information shows the same analysis for another region in the specimen that was cycled 5000 times. A subnanometer thick Pt-Au-rich surface layer is again observed. These results highlight the structural stability of the Pt-Au-Co alloy surface during extended electrochemical cycling.

The role of Au on structural/compositional stabilization can be attributed to a “self-healing” mechanism of Au, which has been previously proposed for PdAu-Pt monolayer core-shell nanoparticles.⁷⁶ Driven by the lower surface energy of Au, the segregated Au atoms toward the surface could potentially stabilize the Pt-Au surface layer, which in turn suppresses the dissolution of Co from the ternary core. This process should be effective for electrochemical cycling potentials that are lower than the standard electrode potential of Au. It should be noted that the Au atoms at the surface contribute little to the measured ECSA, as hydrogen adsorption on Au atoms is negligible relative to Pt.^{47,77} For Pt-Ir-Co, adding Ir is not as efficient as adding Au in suppressing the dissolution of Co, due

to the lower standard electrode potential for Ir in comparison to Au. However, Ir is also useful for stabilizing the activity of Pt-Co. Assuming surface oxide formation and its subsequent chemical dissolution is the mechanism for Pt dissolution, as discussed in ref 78, a reduced rate of Pt dissolution is plausible if the coverage of surface O-containing species could be decreased. As demonstrated in Figures 2 and 3, the Pt-Ir-Co alloy surfaces show weaker binding to oxygen with increasing levels of Ir substitution. Such alloy surfaces are therefore less susceptible to surface oxide formation, leading to a higher resistance to Pt dissolution despite the loss of some Ir with cycling.

CONCLUSIONS

In this study we systematically investigated the ORR activity and the corrosion stability for Pt-Au-Co and Pt-Ir-Co thin film alloys, employing binary Pt-25Co and pure Pt as the baseline. The Pt-2.5 atom % Au-25 atom % Co alloy reaches the peak of the activity volcano with a specific activity of 1.41 mA cm⁻² at 0.95 V, representing an improvement factor of 5 in comparison to the identically synthesized Pt baseline and beating the state-of-the-art Pt-25 atom % Co by 16%. Moreover, the alloys exhibit dramatically improved corrosion stability with increasing levels of Au or Ir substitution. For instance, Pt-10 atom % Au-25 atom % Co shows an initial specific activity of 0.75 mA cm⁻², which is still 2.7 times better than that of pure Pt. Following 100000 potential cycles (0.6–1.0 V) this alloy has only a 25% loss in specific activity, while Pt-25 atom % Co shows an 80% loss. Thus, after 100000 cycles the activity of Pt-10 atom % Au-25 atom % Co is actually 140% higher than that of Pt-25 atom % Co.

ASSOCIATED CONTENT

S Supporting Information

The following file is available free of charge on the ACS Publications website at DOI: 10.1021/cs501710b.

Additional data and information as detailed in the text (PDF)

AUTHOR INFORMATION

Corresponding Authors

*E-mail for X.T.: xtan@ualberta.ca.
*E-mail for D.M.: david.mitlin2@gmail.com.

Notes

The authors declare no competing financial interest.

ACKNOWLEDGMENTS

This research was conducted as part of the Catalysis Research for Polymer Electrolyte Fuel Cells (CaRPE FC) Network administered from Simon Fraser University and supported by Automotive Partnership Canada (APC) Grant No. APCPJ 417858-11 through the Natural Sciences and Engineering Research Council of Canada (NSERC). We acknowledge the technical assistance of the Alberta Cancer Foundation Cell Imaging Facility at the Cross Cancer Institute.

REFERENCES

- (1) Wagner, F. T.; Lakshmanan, B.; Mathias, M. F. *J. Phys. Chem. Lett.* **2010**, *1*, 2204–2219.
- (2) Xing, T.; Zheng, Y.; Li, L. H.; B. Cowie, B. C. C.; Gunzelmann, D.; Qiao, S. Z.; Huang, S.; Chen, Y. *ACS Nano* **2014**, *8*, 6856–6862.
- (3) Wang, Y.; Jiang, X. *ACS Appl. Mater. Interfaces* **2013**, *5*, 11597–11602.
- (4) Snyder, J.; Danilovic, N.; Paulikas, A. P.; Tripkovic, D.; Strmcnik, D.; Markovic, N. M.; Stamenkovic, V. R. *J. Phys. Chem. C* **2013**, *117*, 23790–23796.
- (5) Stephens, I. E. L.; Bondarenko, A. S.; Gronbjerg, U.; Rossmeisl, J.; Chorkendorff, I. *Energy Environ. Sci.* **2012**, *5*, 6744–6762.
- (6) Zhu, G.-Z.; Prabhudev, S.; Yang, J.; Gabardo, C. M.; Botton, G. A.; Soleimani, L. *J. Phys. Chem. C* **2014**, *118*, 22111–22119.
- (7) Su, L.; Jia, W.; Li, C.-M.; Lei, Y. *ChemSusChem* **2014**, *7*, 361–378.
- (8) Kim, K. W.; Kim, S. M.; Choi, S.; Kim, J.; Lee, I. S. *ACS Nano* **2012**, *6*, 5122–5129.
- (9) Xie, J.; Yang, X.; Han, B.; Yang, S.-H.; Wang, D. *ACS Nano* **2013**, *7*, 6337–6345.
- (10) Kok Poh, C.; Hua Lim, S.; Tian, Z.; Lai, L.; Feng, Y. P.; Shen, Z.; Lin, J. *Nano Energy* **2013**, *2*, 28–39.
- (11) van Drunen, J.; Pilapil, B. K.; Makonnen, Y.; Beauchemin, D.; Gates, B. D.; Jerkiewicz, G. *ACS Appl. Mater. Interfaces* **2014**, *6*, 12046–12061.
- (12) Wang, C.; Li, D.; Chi, M.; Pearson, J.; Rankin, R. B.; Greeley, J.; Duan, Z.; Wang, G.; van der Vliet, D.; More, K. L.; Markovic, N. M.; Stamenkovic, V. R. *J. Phys. Chem. Lett.* **2012**, *3*, 1668–1673.
- (13) Greeley, J.; Stephens, I. E. L.; Bondarenko, A. S.; Johansson, T. P.; Hansen, H. A.; Jaramillo, T. F.; Rossmeisl, J.; Chorkendorff, I.; Norskov, J. K. *Nat. Chem.* **2009**, *1*, S52–S56.
- (14) Wanjalal, B. N.; Fang, B.; Shan, S.; Petkov, V.; Zhu, P.; Loukrakpam, R.; Chen, Y.; Luo, J.; Yin, J.; Yang, L.; Shao, M.; Zhong, C.-J. *Chem. Mater.* **2012**, *24*, 4283–4293.
- (15) Liu, Y.; Hangarter, C. M.; Bertocci, U.; Moffat, T. P. *J. Phys. Chem. C* **2012**, *116*, 7848–7862.
- (16) Wang, C.; Markovic, N. M.; Stamenkovic, V. R. *ACS Catal.* **2012**, *2*, 891–898.
- (17) Su, L.; Shrestha, S.; Zhang, Z.; Mustain, W.; Lei, Y. *J. Mater. Chem. A* **2013**, *1*, 12293–12301.
- (18) Choi, S.-I.; Shao, M.; Lu, N.; Ruditskiy, A.; Peng, H.-C.; Park, J.; Guerrero, S.; Wang, J.; Kim, M. J.; Xia, Y. *ACS Nano* **2014**, *8*, 10363–10371.
- (19) Zhang, S.; Zhang, X.; Jiang, G.; Zhu, H.; Guo, S.; Su, D.; Lu, G.; Sun, S. *J. Am. Chem. Soc.* **2014**, *136*, 7734–7739.
- (20) Xie, S.; Choi, S.-I.; Lu, N.; Roling, L. T.; Herron, J. A.; Zhang, L.; Park, J.; Wang, J.; Kim, M. J.; Xie, Z.; Mavrikakis, M.; Xia, Y. *Nano Lett.* **2014**, *14*, 3570–3576.
- (21) Henry, J. B.; Maljusch, A.; Huang, M.; Schuhmann, W.; Bondarenko, A. S. *ACS Catal.* **2012**, *2*, 1457–1460.
- (22) Gan, L.; Heggen, M.; Rudi, S.; Strasser, P. *Nano Lett.* **2012**, *12*, 5423–5430.
- (23) Gan, L.; Heggen, M.; O’Malley, R.; Theobald, B.; Strasser, P. *Nano Lett.* **2013**, *13*, 1131–1138.
- (24) Wang, D.; Yu, Y.; Xin, H. L.; Hovden, R.; Ercius, P.; Mundy, J. A.; Chen, H.; Richard, J. H.; Muller, D. A.; DiSalvo, F. J.; Abruna, H. D. *Nano Lett.* **2012**, *12*, 5230–5238.
- (25) Kuttiyiel, K. A.; Sasaki, K.; Choi, Y.; Su, D.; Liu, P.; Adzic, R. R. *Energy Environ. Sci.* **2012**, *5*, 5297–5304.
- (26) Choi, Y.; Kuttiyiel, K. A.; Labis, J. P.; Sasaki, K.; Park, G.-G.; Yang, T.-H.; Adzic, R. R. *Top Catal.* **2013**, *56*, 1059–1064.
- (27) Chen, C.; Kang, Y.; Huo, Z.; Zhu, Z.; Huang, W.; Xin, H. L.; Snyder, J. D.; Li, D.; Herron, J. A.; Mavrikakis, M.; Chi, M.; More, K. L.; Li, Y.; Markovic, N. M.; Somorjai, G. A.; Yang, P.; Stamenkovic, V. R. *Science* **2014**, *343*, 1339–1343.
- (28) van der Vliet, D. F.; Wang, C.; Tripkovic, D.; Strmcnik, D.; Zhang, X. F.; Debe, M. K.; Atanasoski, R. T.; Markovic, N. M.; Stamenkovic, V. R. *Nat. Mater.* **2012**, *11*, 1051–1058.
- (29) Cui, C.-H.; Li, H.-H.; Liu, X.-J.; Gao, M.-R.; Yu, S.-H. *ACS Catal.* **2012**, *2*, 916–924.
- (30) Strasser, P.; Koh, S.; Anniyev, T.; Greeley, J.; More, K.; Yu, C.; Liu, Z.; Kaya, S.; Nordlund, D.; Ogasawara, H.; Toney, M. F.; Nilsson, A. *Nat. Chem.* **2010**, *2*, 454–460.
- (31) Yang, J.; Yang, J.; Ying, J. Y. *ACS Nano* **2012**, *6*, 9373–9382.
- (32) Prabhudev, S.; Bugnet, M.; Bock, C.; Botton, G. A. *ACS Nano* **2013**, *7*, 6103–6110.
- (33) Stamenkovic, V. R.; Mun, B. S.; Mayrhofer, K. J. J.; Ross, P. N.; Markovic, N. M.; Rossmeisl, J.; Greeley, J.; Norskov, J. K. *Angew. Chem., Int. Ed.* **2006**, *45*, 2897–2901.
- (34) Stephens, I. E. L.; Bondarenko, A. S.; Perez-Alonso, F. J.; Calle-Vallejo, F.; Bech, L.; Johansson, T. P.; Jepsen, A. K.; Frydendal, R.; Knudsen, B. P.; Rossmeisl, J.; Chorkendorff, I. *J. Am. Chem. Soc.* **2011**, *133*, 5485–5491.
- (35) Rothenberg, G. *Catalysis: Concepts and Green Applications*; Wiley-VCH: Weinheim, Germany, 2008; p 65.
- (36) Abild-pedersen, F.; Greeley, J.; Studt, F.; Rossmeisl, J.; Munter, T. R.; Moses, P. G.; Skulason, E.; Bligaard, T.; Norskov, J. K. *Phys. Rev. Lett.* **2007**, *99*, 016105.
- (37) Guo, S.; Li, D.; Zhu, H.; Zhang, S.; Markovic, N. M.; Stamenkovic, V. R.; Sun, S. *Angew. Chem., Int. Ed.* **2013**, *52*, 3465–3468.
- (38) Patrick, B.; Ham, H. C.; Shao-Horn, Y.; Allard, L. F.; Hwang, G. S.; Ferreira, P. J. *Chem. Mater.* **2013**, *25*, 530–535.
- (39) Wang, D.; Xin, H. L.; Hovden, R.; Wang, H.; Yu, Y.; Muller, D. A.; DiSalvo, F. J.; Abruna, H. D. *Nat. Mater.* **2013**, *12*, 81–87.
- (40) Cantane, D. A.; Oliveira, F. E. R.; Santos, S. F.; Lima, F. H. B. *Appl. Catal., B* **2013**, *136*, 351–360.
- (41) Beard, K. D.; Borrelli, D.; Cramer, A. M.; Blom, D.; Van Zee, J. W.; Monnier, J. R. *ACS Nano* **2009**, *3*, 2841–2853.
- (42) Maillard, F.; Dubau, L.; Durst, J.; Chatenet, M.; Andre, J.; Rossinot, E. *Electrochem. Commun.* **2010**, *12*, 1161–1164.
- (43) Dubau, L.; Lopez-Haro, M.; Castanheira, L.; Durst, J.; Chatenet, M.; Bayle-Guillemaud, P.; Guetaz, L.; Caque, N.; Rossinot, E.; Maillard, F. *Appl. Catal., B* **2013**, *142*, 801–808.
- (44) Lopez-Haro, M.; Dubau, L.; Guetaz, L.; Bayle-Guillemaud, P.; Chatenet, M.; Andre, J.; Caque, N.; Rossinot, E.; Maillard, F. *Appl. Catal., B* **2014**, *152*, 300–308.
- (45) Zhang, J.; Vukmirovic, M. B.; Xu, Y.; Mavrikakis, M.; Adzic, R. R. *Angew. Chem., Int. Ed.* **2005**, *44*, 2132–2135.
- (46) Zhang, L.; Iyyamperumal, R.; Yancey, D. F.; Crooks, R. M.; Henkelman, G. *ACS Nano* **2013**, *7*, 9168–9172.
- (47) Wang, C.; van der Vliet, D.; More, K. L.; Zaluzec, N. J.; Peng, S.; Sun, S.; Daimon, H.; Wang, G.; Greeley, J.; Pearson, J.; Paulikas, A. P.; Karapetrov, G.; Strmcnik, D.; Markovic, N. M.; Stamenkovic, V. R. *Nano Lett.* **2011**, *11*, 919–926.
- (48) Yang, J.; Chen, X.; Yang, X.; Ying, J. Y. *Energy Environ. Sci.* **2012**, *5*, 8976–8981.
- (49) Sun, X.; Li, D.; Ding, Y.; Zhu, W.; Guo, S.; Wang, Z. L.; Sun, S. *J. Am. Chem. Soc.* **2014**, *136*, 5745–5749.

- (50) Wang, G.; Huang, B.; Xiao, L.; Ren, Z.; Chen, H.; Wang, D.; Abruna, H. D.; Lu, J.; Zhuang, L. *J. Am. Chem. Soc.* **2014**, *136*, 9643–9649.
- (51) Kang, Y.; Snyder, J.; Chi, M.; Li, D.; More, K. L.; Markovic, N. M.; Stamenkovic, V. R. *Nano Lett.* **2014**, *14*, 6361–6367.
- (52) Loukrakpam, R.; Wanjala, B. N.; Yin, J.; Fang, B.; Luo, J.; Shao, M.; Protsailo, L.; Kawamura, T.; Chen, Y.; Petkov, V.; Zhong, C.-J. *ACS Catal.* **2011**, *1*, 562–572.
- (53) Loukrakpam, R.; Shan, S.; Petkov, V.; Yang, L.; Luo, J.; Zhong, C.-H. *J. Phys. Chem. C* **2013**, *117*, 20715–20721.
- (54) Ma, Y.; Balbuena, P. B. *J. Phys. Chem. C* **2013**, *117*, 23224–23234.
- (55) Jerkiewicz, G. *Electrocatalysis* **2010**, *1*, 179–199.
- (56) Dubau, L.; Maillard, F.; Chatenet, M.; Andre, J.; Rossinot, E. *Electrochim. Acta* **2010**, *56*, 776–783.
- (57) Urchaga, P.; Baranton, S.; Coutanceau, C.; Jerkiewicz, G. *Langmuir* **2012**, *28*, 3658–3663.
- (58) Zhang, L.; Holt, C. M. B.; Luber, E. J.; Olsen, B. C.; Wang, H.; Danaie, M.; Cui, X.; Tan, X.; Lui, V. W.; Kalisvaart, W. P.; Mitlin, D. J. *Phys. Chem. C* **2011**, *115*, 24381–24393.
- (59) Schneider, A.; Colmenares, L.; Seidel, Y. E.; Jusys, Z.; Wickman, B.; Kasemo, B.; Behm, R. *J. Phys. Chem. Chem. Phys.* **2008**, *10*, 1931–1943.
- (60) Nesselberger, M.; Roefzaad, M.; Hamou, R. F.; Biedermann, P. U.; Schweinberger, F. F.; Kunz, S.; Schloegl, K.; Wiberg, G. K. H.; Ashton, S.; Heiz, U.; Mayrhofer, K. J. J.; Arenz, M. *Nat. Mater.* **2013**, *12*, 919–924.
- (61) Shao, M.; Peles, A.; Shoemaker, K. *Nano Lett.* **2011**, *11*, 3714–3719.
- (62) Ruban, A. V.; Skriver, H. L.; Norskov, J. K. *Phys. Rev. B* **1999**, *59*, 15990–16000.
- (63) Weinert, M.; Watson, R. E. *Phys. Rev. B* **1995**, *51*, 17168–17180.
- (64) Hammer, B.; Morikawa, Y.; Norskov, J. K. *Phys. Rev. Lett.* **1996**, *76*, 2141–2144.
- (65) Wakisaka, M.; Mitsui, S.; Hirose, Y.; Kawashima, K.; Uchida, H.; Watanabe, M. *J. Phys. Chem. B* **2006**, *110*, 23489–23496.
- (66) Toda, T.; Igarashi, H.; Uchida, H.; Watanabe, M. *J. Electrochem. Soc.* **1999**, *146*, 3750–3756.
- (67) Jerkiewicz, G.; Vatankhah, G.; Lessard, J.; Soriaga, M. P.; Park, Y.-S. *Electrochim. Acta* **2004**, *49*, 1451–1459.
- (68) Rodriguez, J. A.; Goodman, D. W. *Science* **1992**, *257*, 897–903.
- (69) Stamenkovic, V. R.; Mum, B. S.; Arenz, M.; Mayrhofer, K. J. J.; Lucas, C. A.; Wang, G.; Ross, P. N.; Markovic, N. M. *Nat. Mater.* **2007**, *6*, 241–247.
- (70) van der Vliet, D. F.; Wang, C.; Li, D.; Paulikas, A. P.; Greeley, J.; Rankin, R. B.; Strmcnik, D.; Tripkovic, D.; Markovic, N. M.; Stamenkovic, V. R. *Angew. Chem., Int. Ed.* **2012**, *51*, 3139–3142.
- (71) Stamenkovic, V. R.; Fowler, B.; Mum, B. S.; Wang, G.; Ross, P. N.; Lucas, C. A.; Markovic, N. M. *Science* **2007**, *315*, 493–497.
- (72) Durst, J.; Lopez-Haro, M.; Dubau, L.; Chatenet, M.; Soldo-Olivier, Y.; Guetaz, L.; Bayle-Guillemaud, P.; Maillard, F. *J. Phys. Chem. Lett.* **2014**, *5*, 434–439.
- (73) Cui, C.; Gan, L.; Heggen, M.; Rudi, S.; Strasser, P. *Nat. Mater.* **2013**, *12*, 765–771.
- (74) Ham, H. C.; Manogaran, D.; Lee, K. H.; Kwon, K.; Jin, S.; You, D. J.; Pak, C.; Hwang, G. S. *J. Chem. Phys.* **2013**, *139*, 201104.
- (75) Markovic, N. M.; Ross, P. N. *Surf. Sci. Rep.* **2002**, *45*, 117–229.
- (76) Sasaki, K.; Naohara, H.; Choi, Y.; Cai, Y.; Chen, W.-F.; Liu, P.; Adzic, R. R. *Nat. Commun.* **2012**, *3*, 1115.
- (77) Hu, M.; Linder, D. P.; Nardelli, M. B.; Striolo, A. *J. Phys. Chem. C* **2013**, *117*, 15050–15060.
- (78) Rinaldo, S. G.; Stumper, J.; Eikerling, M. *J. Phys. Chem. C* **2010**, *114*, 5773–5785.